Journal of Power Sources 196 (2011) 7237–7244

Contents lists available at ScienceDirect

Journal of Power Sources

journal homepage: www.elsevier.com/locate/jpowsour

$La_{0.99}Co_{0.4}Ni_{0.6}O_{3-\delta}$–$Ce_{0.8}Gd_{0.2}O_{1.95}$ as composite cathode for solid oxide fuel cells

Per Hjalmarsson*, Mogens Mogensen

Risø National Laboratory for Sustainable Energy, Divison for Fuel Cells and Solid State Chemistry, Technical University of Denmark, Fredrikborgsvej 399, P.O. Box 49, DK-4000 Roskilde, Denmark

ARTICLE INFO

Article history:
Received 11 June 2010
Received in revised form
11 November 2010
Accepted 12 November 2010
Available online 19 November 2010

Keywords:
SOFC cathode
Lanthanum cobalt nickel oxide
Composite oxygen electrode

ABSTRACT

We have studied a new composite SOFC cathode consisting of $LaCo_{0.4}Ni_{0.6}O_{3-\delta}$ (LCN60) and $Ce_{0.9}Gd_{0.1}O_{1.95}$ (CGO). The polarisation resistance (R_P) at 750 °C and OCV was measured to $0.05 \pm 0.01\ \Omega\,cm^2$ and the activation energy was determined to be about 1 eV. The impedance spectra were modelled with an EQC model consisting of a high frequency Z_{RQ} circuit and a medium frequency Gerischer impedance, Z_G. The resistance of Z_G was found to decrease with approximately a factor of two as a consequence of infiltration of $(La_{0.6}Sr_{0.4})_{0.99}CoO_3$ into the porous LCN60–CGO structure. R_P of both infiltrated and non-infiltrated LCN60–CGO cathodes is substantially lower than that of LSM–YSZ and comparable with single phase LSC cathodes at low T due to its low E_A. R_P was also found to be stable at 750 °C and OCV. The cathodes were integrated onto ScYSZ based anode supported cells which were measured to have an ASR of 0.16–0.18 $\Omega\,cm^2$ at 750 °C.

1. Introduction

$LaCo_{1-x}Ni_xO_{3-\delta}$ (LCN) with $x = 0.4$ or 0.6 has been reported to possess high electronic conductivity and a thermal expansion coefficient (*TEC* is ~14–17 × $10^{-6}\ K^{-1}$) that is relatively well matched to a SOFCs. Yet it has still received surprisingly little attention in the context of SOFC electrode material [1].

$LaCoO_3$ has complex electronic and magnetic properties due to the thermally excited transitions from low/intermediate spin ($t_{2g}^6/t_{2g}^5\ e_g^1$) to high spin ($t_{2g}^4\ e_g^2$) that occur on the Co^{3+} when positioned in the octahedral site of the crystal structure [2]. This results in an insulator to semi conductor transition with high electronic conductivities at SOFC operating temperatures but also a high *TEC* of about 22 × $10^{-6}\ K^{-1}$ as a result of the expansion of the Co ion radius [3–6]. This is twice that of the other SOFC components and the mismatch poses mechanical problems upon thermal cycling. In $LaNiO_3$ no such transitions have been reported and the *TEC* is only about 10 × $10^{-6}\ K^{-1}$ [7]. Furthermore, the Ni^{3+} ion in $LaNiO_3$ has one electron found in the delocalised *itinerant* conduction band ($t_{2g}^6\ e_g^1$) which makes this crystal a *n*-type metallic-like conductor [8]. $LaNiO_3$ starts to decompose above 850 °C but the crystal is stabilised by partial substitution of Co [7,9]. $LaCo_{1-x}Ni_xO_3$ is for these reasons an interesting perovskite material for SOFC cathode applications.

$La_{0.99}Co_{0.6}Ni_{0.4}O_{3-\delta}$ (LCN40) has previously been studied at Risø-DTU for this purpose. In this study the electronic conductivity of LCN40 was found to be 1200–1500 $S\,cm^{-1}$ from room temperature to 1000 °C [9]. The *TEC* was on the other hand measured to 17.3 × $10^{-6}\ K^{-1}$ which is rather high when matched to that of the other components. More importantly the electrochemical performance when using LCN40 as a porous SOFC cathode was very poor with a high polarisation resistance (R_P) of $20 \pm 5\ \Omega\,cm^2$ at 750 °C [9]. It was reported in the aforementioned study that LCN40 requires temperatures above 1000 °C to desorbs oxygen and create the oxygen vacancies (δ) required for materials with considerable oxide ion conductivity. The lack of such vacancies was further suggested as a potential reason for the low performance of porous single phase LCN40 cathodes.

In order to improve the properties of $La_{0.99}Co_{1-x}Ni_xO_{3-\delta}$ as SOFC cathode material three actions were taken. (1) x was increased to 0.6 in order to decrease the *TEC* and increase the conductivity. (2) The acquired powder of $La_{0.99}Co_{0.4}Ni_{0.6}O_{3-\delta}$ (LCN60) was mixed with $Ce_{0.9}Gd_{0.1}O_{1.95}$ (CGO) into a composite electrode. (3) The LCN:CGO composite electrode was infiltrated with a mixed conducting material (LSC40). The principle idea behind this structure is that the LCN phase will provide the electronic conductivity, the CGO phase will provide the ionic conductivity and the LSC phase will provide the catalytic activity.

We will here report electrochemical data measured on this electrode and discuss its applicability as an SOFC cathode on basis of: (1) material properties including electronic conductivity and expansion properties. (2) Electrode polarisation resistance measured with impedance spectroscopy on a symmetrical cell configuration.

* Corresponding author. Tel.: +45 4677 5759; fax: +45 4677 5758.
E-mail address: phja@risoe.dtu.dk (P. Hjalmarsson).

0378-7753/$ – see front matter © 2010 Elsevier B.V. All rights reserved.
doi:10.1016/j.jpowsour.2010.11.065

(3) Performance of anode supported cells when using LCN60–CGO as cathode.

2. Experiments

Powder of $La_{0.99}Co_{0.4}Ni_{0.6}O_{3-\delta}$ (LCN) was synthesized using the glycine–nitrate combustion route [10]. Metal nitrate of ($La(NO_3)_3{\cdot}6H_2O$, $Sr(NO_3)_2$, $Co(NO_3)_2{\cdot}6H_2O$ and $Ni(NO_3)_2{\cdot}6H_2O$) were diluted in deionised water and mixed with glycine to give a glycine–nitrate molar ratio of 0.548. The solution was heated to evaporate water and initiate the reaction. This produced a fine powder which was finally calcined at 950 °C for 2 h. About 300 mg of powder sample was heated and cooled in 50 ml min^{-1} airflow to 1300 °C using a A NETZSCH STA 409C/CD in order to determine oxygen non-stoichiometry as a function of temperature. The powder was shaped into bars, isostactically pressed 30 s at 325 MPa and sintered again at 1250 °C. XRD (STOE Theta-Theta diffractometer, 40 kV, 30 mA, Cu Kα-radiation) was employed to confirm the perovskite phase and detect any possible secondary phases.

Powder of $Ce_{0.9}Gd_{0.1}O_{1.95}$ (CGO) was mixed with the LCN60 powder and dispersed into an ink. The ink was screen printed onto both sides of a 200 μm thick and 50 mm × 50 mm large CGO electrolyte and sintered at 1000 °C for 2 h. The cell was cut into small samples of approximately 5 mm × 5 mm. Four of these cells were subsequently infiltrated a single time with a solution consisting of a surfactant and metal nitrates with a cation molar ratio corresponding to $(La_{0.6}Sr_{0.4})_{0.99}CoO_3$. The infiltration methodology is described elsewhere [11].

The conductivity was measured with a standard 4 point probe DC-technique. Pressed and sintered bars of above 95% theoretical density were painted with platinum paste and wired with platinum threads at both ends. The resistance was measured with a Keithley 2700 multimeter. Voltage probes were separated 6.8 mm apart and measurements were performed at temperatures ranging from 50 to 950 °C at ambient P_{O_2}.

The LCN60–CGO ink was also screen printed onto 53 mm × 53 mm large anode supported SOFCs which consisted of a Ni-YSZ support, Ni-ScYSZ cermet anode, ScYSZ electrolyte and a wet deposited CGO barrier [12]. The cathode was sintered in the same way as for the symmetrical cells. One cell was subsequently infiltrated twice using the $(La_{0.6}Sr_{0.4})_{0.99}CoO_3$ solution with an intermediate heating to 350 °C in order to combust organics and nitrates.

Four identical symmetrical cells with both infiltrated and non-infiltrated cathodes were measured with electrochemical impedance spectroscopy (EIS) using a Solartron-1260 frequency response analyzer and the test setup described in Fig. 1. The measurements were carried out at open circuit voltage (OCV), under an ambient air flow of 6 lh^{-1} and from 550 to 850 °C and then to 550 °C (see Fig. 1). Data were treated with a linear least square fit program, ZsimpWin3.21. An algorithm to extract the distribution of relaxation times (DRT) of the measured and fitted impedance was used in order to support the choice of equivalent circuit model (EQC) [13]. All resistances are reported with a 95% confidence interval based on the four measured samples.

The anode supported cells were tested in the Risø-DTU SOFC test setup described elsewhere [14]. Glass frames were used to assemble the anode and cathode gas flow compartments. The cells were contacted with corrugated Ni- and Au-mesh on the anode and cathode side respectively. The cells were heated to 850 °C before 0.5 kg^{-1} cm^2 of weight was applied in order to compress the sealing and ensure electric contact. The anode was then reduced with 9% H_2 in N_2 for 2 h followed by 1 h in H_2 containing approximately 4% humidity. The cells were tested from 850 to 650 °C with 50 °C increments using *i–v* polarisation and EIS measurements under air and O_2 on the cathode side and under 4% and 20% humidity on the anode side. Flows were set to 140 lh^{-1} of air and 24 lh^{-1} of H_2. We have also conducted systematic shifts in the oxygen and fuel partial pressure in order to study the impedance response of the two electrodes in more detail.

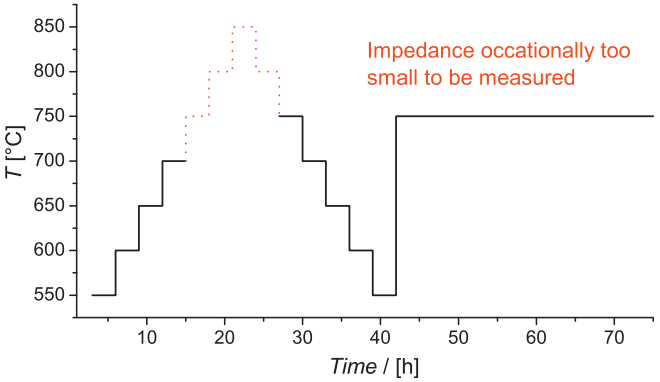

Fig. 1. Temperature profile during symmetrical cell test experiments.

3. Result and discussion

Fig. 2 plots the XRD pattern of the LCN60 and shows a single phase material within the detection limit of the technique. It shows further a hexagonal crystal structure with lattice parameters a_{hex} = 5.46 Å and and c_{hex} = 13.14 Å. This is in close agreement with [1] when converting from rhombohedral to hexagonal lattice parameters.

Fig. 3 plots the oxygen nonstoichiometry factor, δ, as function of temperature for LCN40 and LCN60. It indicates that the onset temperature of oxygen formation is above 950–1000 °C and that these compositions are fully stoichiometric in the operating temperature range of SOFCs.

Fig. 4 plots the electric conductivity of LCN40 and LCN60 from room temperature to ~1000 °C. It shows that LCN60 exhibits metallic like conductivity whereas LCN40 shows a typical small polaron conduction behavior. The total conductivity of both compositions is substantially higher than that of the conventional cathode material LSM ($(La_{1-x}Sr_x)_sMnO_3$ $0.2 < x < 0.3$; $0.9 < s < 1$) which is just below 200 S cm^{-1} at 800 °C [15,16]. Huang et al. have measured the *TEC* of LCN60 to 14.3 K^{-1} for the temperature region 25–850 °C [1]. *TEC* of CGO10 is approximately 12.2 K^{-1} [17] and thus the effective

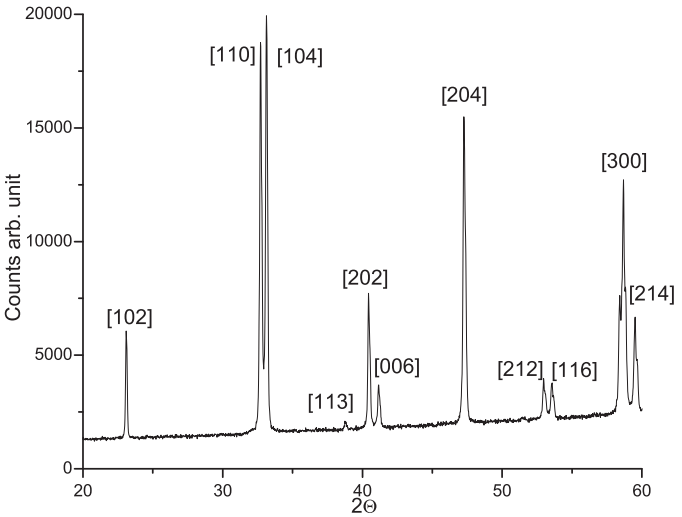

Fig. 2. Powder XRD of LCN60 at room temperature and ambient air.

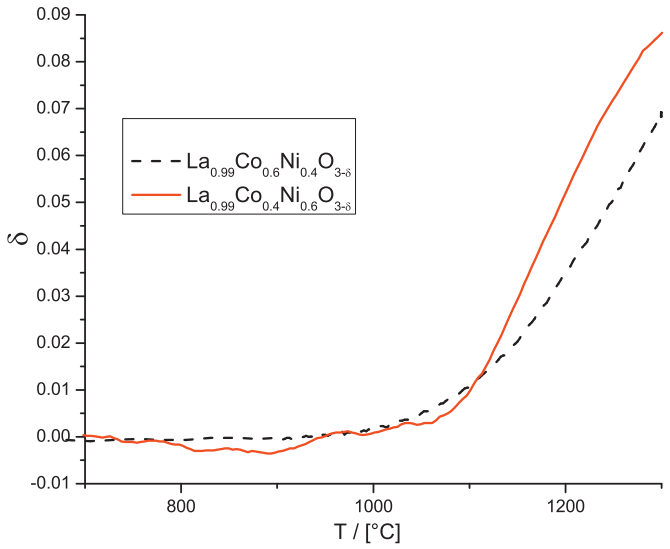

Fig. 3. Thermograviometric data showing the oxygen nonstoichiometry coefficient, δ, as function of T in ambient air.

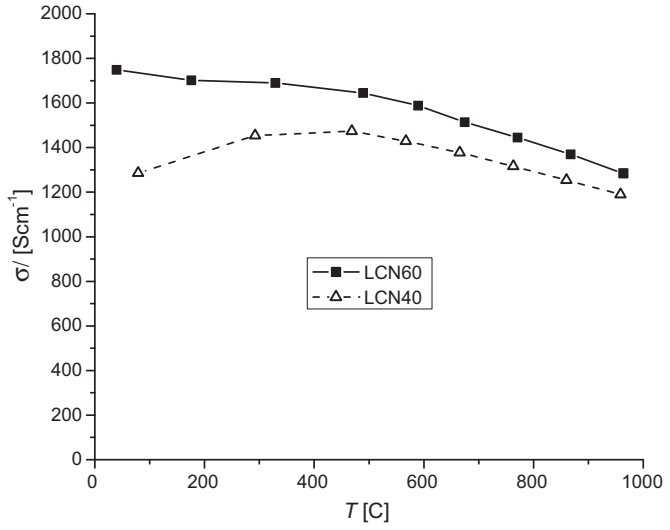

Fig. 4. Electrical conductivity of LCN40 and LCN60 as function of temperature in ambient air.

expansion of an LCN60–CGO10 composite cathode will be matched relatively well to the rest of the cell.

In recent years LSCF ($(La_{0.6}Sr_{0.4})_sCo_{0.2}Fe_{0.8}O_{3-\delta}$) has been proposed as a candidate material for SOCF cathode application. This material has good mixed conducting properties due to its oxygen substochiometry at SOFC operating temperatures [18]. The *TEC* is on other hand slightly higher than that of LCN60 and the electronic conductivity is significantly lower as shown in Table 1 [19]. $(La_{0.6}Sr_{0.4})_sCoO_{3-\delta}$ (LSC40) is another well known cathode material with good electrocatalytic activity towards oxygen reduction [20]. It has a very high electronic conductivity but also a comparably high apparent *TEC* due to both the electronic spin transition and in particular to the thermal reduction of Co^{4+} to Co^{3+} [21]. Table 1 demonstrates that LCN60 has competitive materials properties for use in SOFC cathodes.

Table 1
TEC and conductivity of widely studied SOFC cathode perovskite materials.

Composition	*TEC* [K^{-1}] 25–850 °C	σ [S cm^{-1}] 800 °C
$(La_{0.75}Sr_{x0.25})_sMnO_3$	12.2 [16]	~200 [15,16]
$(La_{0.6}Sr_{0.4})_sCo_{0.2}Fe_{0.8}O_{3-\delta}$	15.4 [19]	~300 [19]
$LaCo_{0.4}Ni_{0.6}O_{3-\delta}$	14.3 [1]	~1400
$(La_{0.6}Sr_{0.4})_sCoO_{3-\delta}$	~20 [9]	~2000 [9]

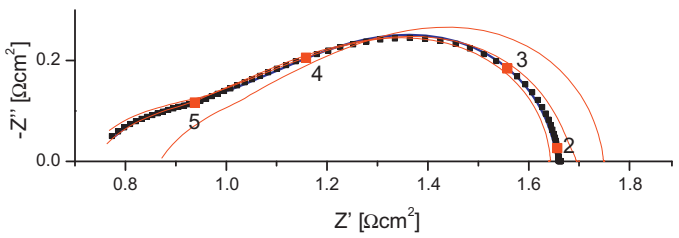

Fig. 5. Four Nyqvist plots of impedance spectra recorded at 550 °C on symmetrical cells with LCN/CGO cathodes. Numbers represent $^{10}\log f$. Blue lines represent the best linear least square fit the EQC model used. (For interpretation of the references to color in this figure legend, the reader is referred to the web version of the article.)

Figs. 5 and 6 show the measured impedance at 550 °C for the four symmetrical cells with infiltrated and non-infiltrated LCN60–CGO cathodes. The plots verify that the measured impedance responses of the four individual samples are similar and indicate that we have reasonable statistics from our measurements. The impedance response does not consist of only one single semi-circle (*RQ*-element). This implies that the overall electrode reaction consists of several processes that occur on different time scales and contribute significantly to the total electrode polarisation resistance. The impedance spectra were analysed in more detail by employing the method of equivalent circuit models (EQC). When applying such models it is good practice to use as few circuits as possible that still give an accurate fits to measured data. Moreover, the model should have a physical meaning in the sense that individual circuits correspond to single electrode processes and that the entire circuit model corresponds to the total electrode kinetics.

The *RQ* circuit is often used to describe electrode reaction steps such as charge transfer across an interface [22] but other circuits exist as well. Adler has shown that two of the major kinetic processes of the oxygen electrode, the oxygen exchange and oxide ion diffusion can be coupled into a single *Gerischer* impedance response [23]. The general *Gerischer* impedance is expressed in Eq. (1) where K_A is a "rate constant" and Y_0 is the admittance.

$$Z_G = \frac{1}{Y_0\sqrt{(K_A + i\omega)}} = \frac{R_G}{\sqrt{1 + i\omega R_G C_G}} \quad (1)$$

Such an impedance response has been argued to arise in both mixed electronic and ionic conducting electrodes (MIEC) such as $La_{1-x}Sr_xCoO_3$ (LSC) [24], in apparent "three phase boundaries" electrodes such as Pt/YSZ [25–27] as well as in LSM/YSZ electrodes when polarized [28]. We have here applied a model with an inductor (L) and a resistor (R_S) in series with [28,29] either two *RQ* circuits (L-R_S-(RQ)-(RQ)) or one *RQ* and one Gerischer circuit (L-R_S-(RQ)-G). The serial resistance (R_S) is assumed to be made up almost exclu-

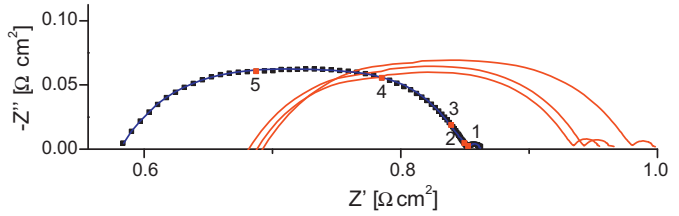

Fig. 6. Four Nyqvist plots of impedance spectra recorded at 550 °C on symmetrical cells with LCN/CGO cathodes infiltrated with LSC40 particles. Numbers represent $^{10}\log f$. Blue lines represent the best linear least square fit the EQC model used. (For interpretation of the references to color in this figure legend, the reader is referred to the web version of the article.)

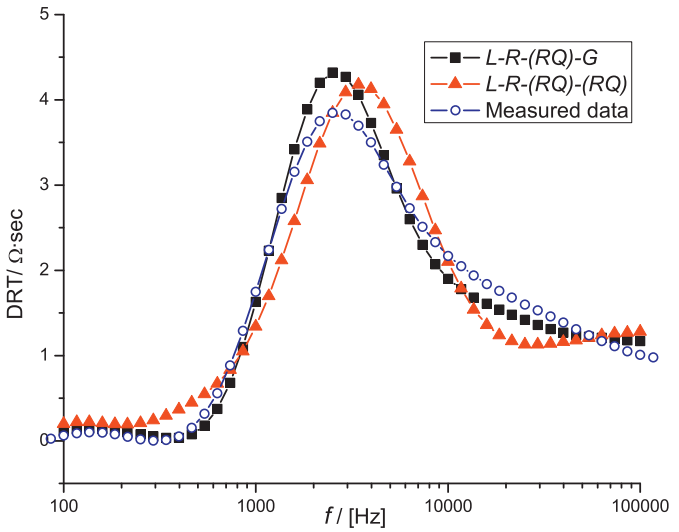

Fig. 7. Shows the distribution of relaxation times (DRT) for the measured impedance as well as the DRT of the impedance reconstructed from modelling the measured impedance using two equivalent circuit models.

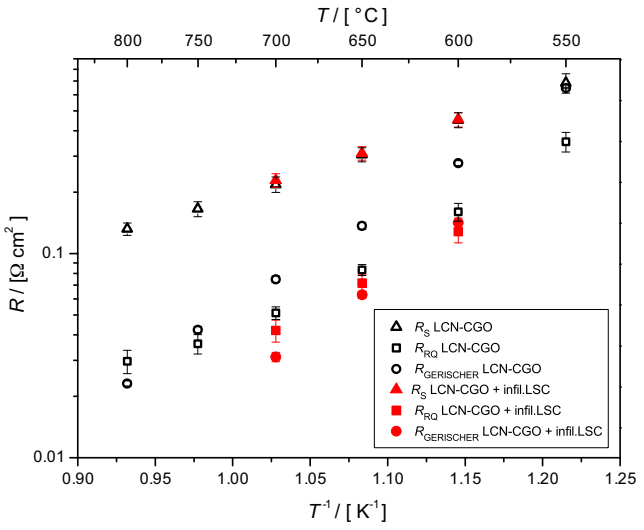

Fig. 9. Arrhenius plot of R_S, R_{RQ} and R_G of the infiltrated and non-infiltrated LCN60–CGO cathodes. Data are taken from the cooling ramp of the EIS measurement procedure. It shows that it is mainly the Z_G impedance response that decreases as a consequence of the LSC infiltration. The activation energies appear to be unaffected by the infiltration.

sively of the ionic resistance of the CGO electrolyte. The n parameter of the high frequency RQ circuit was fixed at 0.5 for all fits.

$$Z_{RQ} = \frac{1}{(1/R_{RQ}) + C_{RQ}(i\omega)^n} \quad (2)$$

In order to properly fit the impedance measured on the LSC infiltrated cells at the first four temperatures of the experiment we also had to include a RC circuit to account for the small semicircle seen at low frequencies. The fact that it had a high capacitance above 10 F could indicate that this is related to oxygen diffusion [30]. It disappeared when the cells were *in situ* heated to temperatures above 700 °C and did not show up again after the experimental thermal cycle to 850 °C. This RC circuit will therefore not be discussed further in this paper. The lines in Figs. 5 and 6 show the best linear least square fit to measured data at 550 °C using the L-R_S-(RQ)-G model. Measured data at higher temperatures were found to fit this model even better. The L-R_S-(RQ)-G circuit turned out to be the most accurate model giving the smallest error. This choice of model was also supported by DRT analysis as argued below.

Fig. 7 shows the DRT of the measured impedance as well as the DRT of the impedance derived from the parameters of the two EQC fits. It displays that the main DRT peak of the (L-R_S-(RQ)-(RQ)) model is shifted towards high frequencies relative to that of the measured data. The DRT of the (L-R_S-(RQ)-G) model on other hand resembles the shape of the measured data quite well. Fig. 8 visualizes how the individual EQC elements of the L-R_S-(RQ)-G model make up the measured impedance spectra. It shows that Z_{RQ} is found at rather high frequencies, which makes this response susceptible to inductive interference inevitably arising from the test setup. The

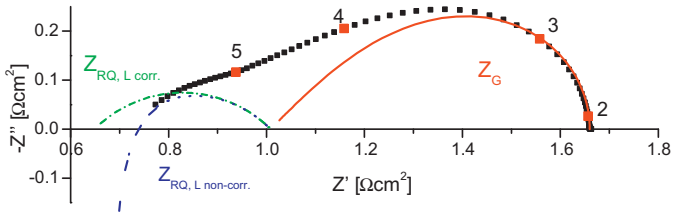

Fig. 8. The EQC model used in the treatment of all the data. Blue dotted lines are extrapolated data to visualize the inductive effect. (For interpretation of the references to color in this figure legend, the reader is referred to the web version of the article.)

inductance could be determined quite precisely at high temperature to about 6.5×10^{-8} F and was found to be almost independent on temperature. Values of the Z_{RQ} response reported here are corrected for this inductance.

Fig. 9 plots the R_S, R_{RQ} and R_G of the cells with infiltrated and non-infiltrated LCN60–CGO cathodes measured during the incremental cooling ramp of the experiment (see Fig. 1). The graph shows that the temperature dependence is slightly different between R_{RQ} and R_G. The resistance of the Gerischer impedance response (R_G) was found to follow an apparent Arrhenius temperature dependence across the entire T range with an activation energy of 0.97 ± 0.01 eV for non-infiltrated cells and 1.12 ± 0.04 eV for the infiltrated cathodes. The resistance of high frequency response (R_{RQ}) did not show an equally clear Arrhenius behavior. The activation energy in the region 550 °C $\leq T \leq$ 700 °C was calculated to 0.85 ±0.06 eV for the non-infiltrated and 0.82 ± 0.07 eV for the infiltrated cathode. Above 750 °C, the temperature dependence of R_{RQ} appears to deviate from a Arrhenius dependence and is much less temperature dependent. The activation energy of the CGO electrolyte resistance (R_S) was found to be 0.49 ± 0.06 eV.

The fact that the activation energy of both two EQC circuits appear to be relatively unaffected could indicate that the reaction mechanism is not dramatically altered by the infiltration of LSC nano-particles.

The capacitance of the high frequency Z_{RQ} response (C_{RQ}) was calculated to approximately 1 μF irrespective of whether the electrode was infiltrated or not. The capacitance associated with the Z_G (C_G) response was calculated to about 30 μF for the non-infiltrated cathode and about 60 μF for the infiltration cathode. Neither the C_G nor the C_{RQ} was found to be dependent on temperature.

The fact that it is only the Z_G response that changes when the surface is modified using infiltrated LSC nano-particles indicates that this impedance is associated with the surface exchange reaction. As discussed earlier, the Gerischer impedance arises in systems where an electrochemical reaction is coupled to an oxide diffusion process [31]. However the diffusion can occur along different pathways, through the bulk, at the surface or a combination of the two. In MIEC cathodes such as LSC40 it has been argued that the oxide ion diffusion occurs primarily along the bulk path due the high oxygen substoichiometry [24]. This gives rise to a relative high capacitance ranging up to 1 F cm^{-2}, as a result of stoichiometric

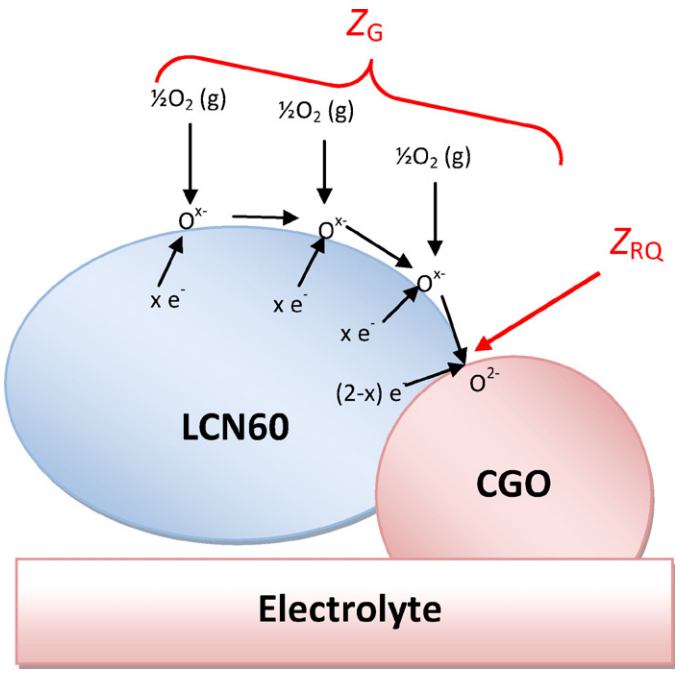

Fig. 10. The proposed reaction mechanism in which the O_2 is reduced and transported at the surface towards the TPB. The charge of the surface oxide specie and the diffusion length is unknown.

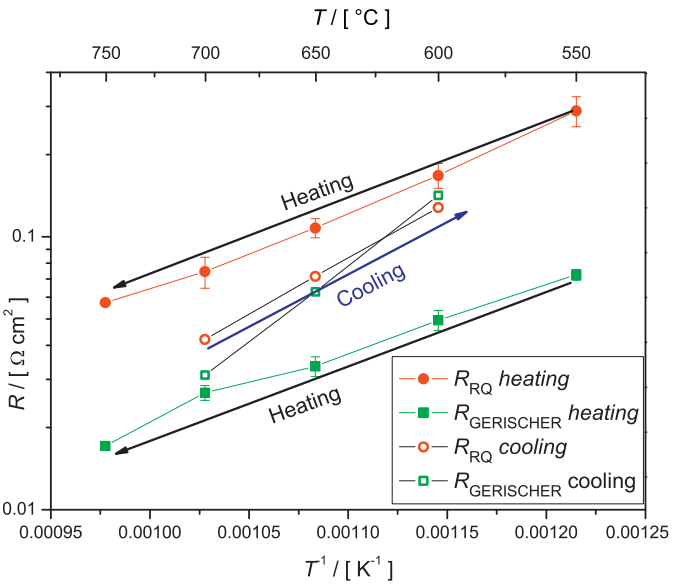

Fig. 11. Arrhenius plot of R_{RQ} and R_G of the infiltrated LCN60–CGO cathodes from both the heating and the cooling ramp of the EIS measurement procedure. R_{RQ} was found to decrease whereas R_G was found to increase as a result of the thermal cycles. Also the apparent activation energy was found to be higher after the 850 °C.

changes in the oxygen sub lattice [25,32]. However the Gerischer capacitance, C_G, of the LCN60–CGO cathode is much lower indicating that the LCN60 bulk is inactive to oxygen stoichiometric changes and thus ionic conduction. Mitterdorfer et al. have found a Gerischer-like impedance for the LSM–YSZ electrode after "correcting" it for a double layer capacitance using the model of Berthier [33]. The capacitance of this Gerischer response was measured to about 100 μF which is close to the C_G measured in this study [34]. This points towards the ionic transport being confined to the surface rather than the bulk.

For electrodes in which oxide ion diffusion is believed to be confined to the surface rather than through the bulk, transfer of O^{2-} across the electrode/electrolyte interface has been argued to occur within a narrow depth close to the TPB [35]. This stand in contrast to MIEC electrode, in which a much larger fraction of the electrode–electrolyte interface is active for O^{2-} charge transfer. Several papers on the related cathode LSM–YSZ have argued that the ionic charge transfer from the electrode to the electrolyte contributes to the resistance of this cathode [36]. The capacitance of such a reaction step is similar to the Z_{RQ} of LCN60–CGO and we therefore speculate that this impedance response is related to O^{2-} transfer occurring at the electrode/electrolyte interface close to the TPB.

A hypothetic reaction mechanism is thus proposed in Fig. 10 in which full or partial oxygen reduction occurs at the LCN60 surface. This reaction is coupled to a surface diffusion that is driven by the depletion of oxide ions at the TPB. It should be stressed that this mechanism holds for OCV conditions only and that the overall process might include a substantial bulk diffusion contribution when polarized as has been argued for the LSM–YSZ cathode [30,32,33,37].

Fig. 11 shows the Arrhenius plot of R_{RQ} and R_G of the infiltrated LCN60–CGO cathode from both the incremental heating and cooling section of the EIS experiment (see right graph of Fig. 1). In order to distinguish between these resistances we will here refer to them as R_{COOL} and R_{HEAT}. Interestingly it shows that R_{RQ} decreases as a result of the thermal cycle to 850 °C. When returning to 700 °C the resistance is only half of what it was prior to the heat treatment. Additionally, the activation energy calculated from the resistance measured during the incremental heating ramp, $R_{RQ,HEAT}$, was found to be 0.62 ± 0.03 eV. This is notably lower than the E_A of 0.82 ± 0.07 eV calculated from $R_{RQ,COOL}$. This effect appears to be even more pronounced for the Z_G response. E_A of R_G is only 0.47 ± 0.03 eV when calculated to from the $R_{G,HEAT}$ values which is less than half of the E_A of 1.12 ± 0.04 eV calculated from the $R_{G,COOL}$ values. R_G was, on the contrary to R_{RQ}, found to increase as a consequence of the *in situ* 850 °C heat treatment.

There are several plausible reasons to why R_{RQ} decreases as a result of the *in situ* heat treatment including (1) better contact between the catalytic nano-particles and the ionic conducting phase or (2) the nano-particles acting as sinks for impurities at the TPB and thus cleaning the charge transfer interface [38]. However, an important effect that one needs to be considered first is that the perovskite phase does not exist from the beginning but crystallizes *in situ* during heating. Teraoka et al. [39,40] have shown that nano-crystalline powder of $(La_{0.8}Sr_{0.2})_{0.99}CoO_3$ synthesized using a method that is similar to our infiltration technique requires temperatures of above 850 °C to form a single phase perovskite. This indicates that the LSC nano-particles are likely synthesized *in situ* during heating and that the degree to which the perovskite phase is formed will increase during the experiment. This will in turn have positive implications on the electrochemical performance of the cathode.

The increase in R_G is most likely due to the growth of the nano-particles which is known to decrease their electocatalytic activity. The reason for the different apparent activation energies could be related to morphological changes and growth of the nano-particles which lowers both its intrinsic activity and the surface area available for the oxygen exchange reaction.

Fig. 12 plots the total electrode polarisation resistance, R_P of the two studied electrodes as well as a number of other electrode types. The comparison shows that R_P of the LCN60–CGO cathode is more than 100 times lower than the pure $La_{0.99}Co_{0.6}Ni_{0.4}O_3$ cathode. Also the activation energy of R_P is substantially lower with about 1 eV for LCN60–CGO and 1.8 eV for LCN40. The LCN composition of the two electrodes is slightly different but the LCN powder synthesis and treatment has been essentially the same [9]. We find it hard to

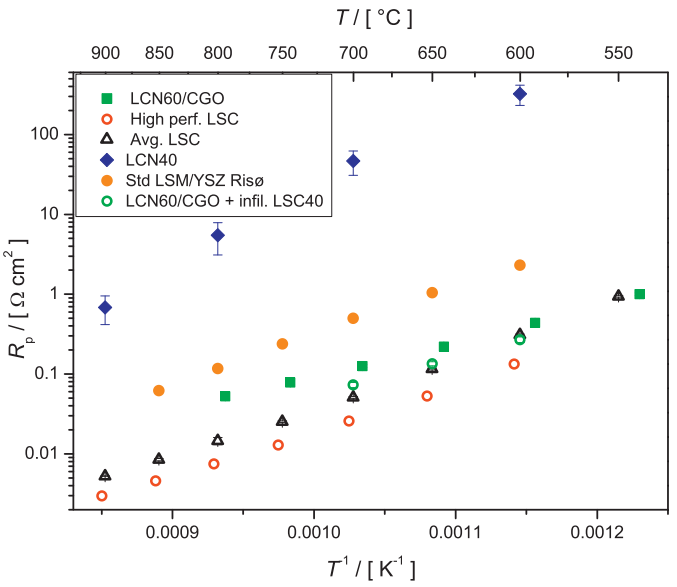

Fig. 12. Comparison of R_P of the two measured electrodes with a selected number of other electrode types. All cathodes have been manufactured at Risø-DTU [41].

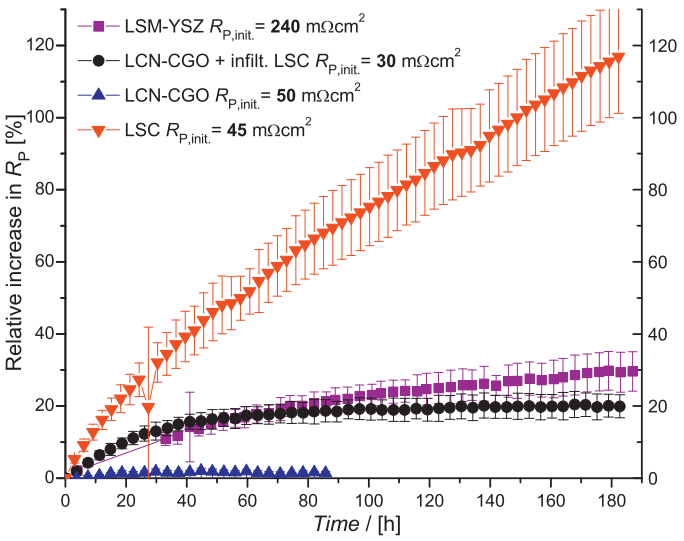

Fig. 13. Relative increase in R_P in air flow at OCV and 750 °C. The infiltrated and non-infiltrated LCN60–CGO cathodes appear to be more stable than both the LSC and LSM–YSZ cathodes.

believe that such a small difference in Ni/Co ratio will have such a pronounced effect on R_P. Instead, this supports the hypothesis of the aforementioned study that ionic transport restricts the overall reaction process of $LaCo_{1-x}Ni_xO_3$ and that this material benefits from being used in composite with an ionic conductor such as CGO. This indicates further that the reaction is likely confined to the vicinity of the three phase boundary (TPB) which makes the LCN60–CGO cathode mechanistically related to the conventional LSM–YSZ electrode ($La_{0.75}Sr_{0.25}Mn_{1.05}O_3$–8YSZ).

Fig. 12 shows further that the LCN60–CGO cathode has a substantially lower R_P than the standard LSM–YSZ electrode of Risø-DTU [41]. The difference is especially pronounced at low temperatures as R_P of the LCN60–CGO cathode has a lower activation energy than the E_A of 1.2 eV for LSM–YSZ. Fig. 12 plots also the R_P of an average $(La_{0.6}Sr_{0.4})_{0.99}CoO_3$ (LSC40) cathode [30]. This MIEC cathode has lower a R_P in the operating temperature range of typical SOFCs. However, the E_A of this LSC40 was also found to be higher than LCN60–CGO (~1.2 eV) which causes a cross-over in R_P somewhere at 550–600 °C.

It is well known that the performance of cathodes is to a large extent dependent on microstructural and morphological properties. This is also explicit in Fig. 12 which shows a single phase LSC40 cathode with a more optimised microstructure that has a R_P of approximately half that of the average LSC40 cathode [30]. This LSC cathode has thus a substantially lower performance than LCN60–CGO even at low temperatures. It should be stressed in this context, however, that the manufacturing of this LCN60–CGO cathode is not yet optimised and that the performance could possibly be enhanced further by tailoring its microstructure.

Fig. 13 plots the relative increase in R_P at OCV and 750 °C under flow of ambient air from a compressed air source. It shows that R_P of the infiltrated LCN60–CGO cathode was measured to increase with about 20% over the first 80 h after which it stabilised. Fig. 13 shows further that R_P of the non-infiltrated LCN60–CGO cathodes did not exhibit a statistically measureable increase within the first 90 h. These results stand in contrast to the measured stability of the both the LSC and LSM–YSZ cathodes as both these electrodes showed a continuous increase in R_P over the measured period with LSC doing so dramatically more pronounced. There are numerous potential degradation mechanisms which can be driven by thermodynamic, electrostatic or mechanical driving forces. Due to the many different possible degradation mechanisms it is therefore very difficult to interpret the differences in degradation rates between these different cathodes. It is furthermore important to keep in mind the relatively short period for which the stability of these cells has been tested. However, irrespective of the origin of the degradation this cathode it is technologically interesting that the LCN60–CGO cathode does not seem to undergo any a short term thermodynamic or microstructural changes that affect its electrochemical performance. The initial degradation of the LSC infiltrated LCN60–CGO cathode is most likely related to the nano-particles themselves. Whether this is associated with the microstructural (e.g., particles growth), thermodynamic (e.g., cation redistribution) or morphological (e.g., crystallisation) is more difficult to establish and more focus on this aspect is needed in order to evaluate this new manufacturing technique for the next generation of high performance cathodes.

Fig. 14 plots the i–v- and power characteristics at 750 °C for four anode supported SOFCs. Two of the cells had the infiltrated and non-infiltrated LCN60–CGO cathodes and two cells had the LSC–CGO

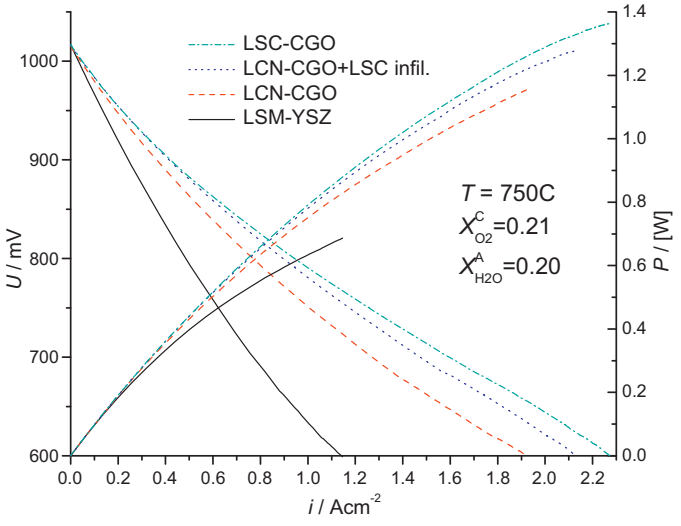

Fig. 14. Shows four i–v- and power curves for anode supported cells measured at 750 °C and $X^C_{O_2} = 0.21$ and $X^A_{H_2O} = 0.20$.

Table 2
ASR, R_P and R_S values from the tests shown in Fig. 14. $T = 750\,^{\circ}C$; $X^{C}_{O_2} = 0.21$ and $X^{A}_{H_2O} = 0.04$.

Cell	ASR_{corr} [$\Omega\,cm^2$]	$R_{S,OCV}$ [$\Omega\,cm^2$]	$R_{P,OCV}$ [$\Omega\,cm^2$]
LSC–CGO	0.15	0.06	0.30
LCN60–CGO	0.18	0.09	0.28
LCN60–CGO + LSC infilt	0.16	0.08	0.26
LSM–YSZ	0.33	0.13	0.40

and LSM–YSZ cathodes. All half cells were manufactured similarly as described in the experimental section with the difference that the LSM–YSZ cathode was screen printed directly onto the ScYSZ electrolyte and did thus not have a CGO barrier. Fig. 14 shows that the higher performance of the LCN60–CGO cathode as compared to the LSM–YSZ can be seen also in a full SOFC test.

Table 2 lists the area specific resistance calculated from *i–v* polarisation curves, corrected for fuel utilization according to Ref. [14]. It also tabulates the serial (R_S) and polarisation (R_P) resistance extracted from EIS measurements at OCV. Table shows that R_P of the two LCN60–CGO cells and the LSC–CGO cell is quite similar. The major difference, at least on a relative scale, is instead the R_S which is 50% higher for the LCN60–CGO cell as compared to the LSC–CGO. There seems to be a rather strong correlation between the R_S and ASR_{corr} with a better electronic conducting cathode giving rise to both a lower serial and total cell resistance.

Figs. 15 and 16 plot DRT analysis of the LCN60–CGO cell at different oxygen and fuel partial pressures on the cathode and anode side respectively. The figures show that the major impedance response of R_P at 100–1000 Hz is almost exclusively associated with the anode side of the cell. It shows further that the low frequency response below 10 Hz is also exclusively associated with the anode and that it is only a small response at 20–50 Hz that can partially be ascribed to the cathode. This indicates that the cathode contribution to R_P is comparatively small in these cells. On the contrary, R_P of the LSM–YSZ cell is significantly higher indicating an additional contribution to R_P. It is also known from earlier studies that the LSM–YSZ cathode gives rise to substantial resistance at 750 °C in ScYSZ based ASC [42].

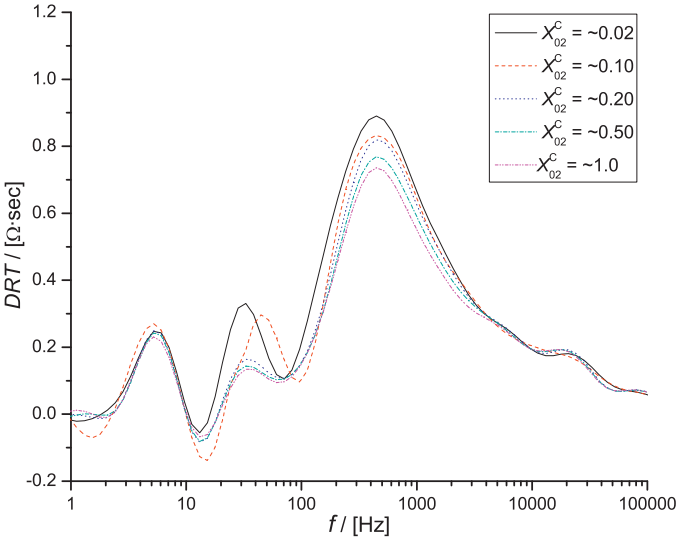

Fig. 15. DRT analysis the impedance measured at OCV, 650 °C and different cathode P_{O_2}.

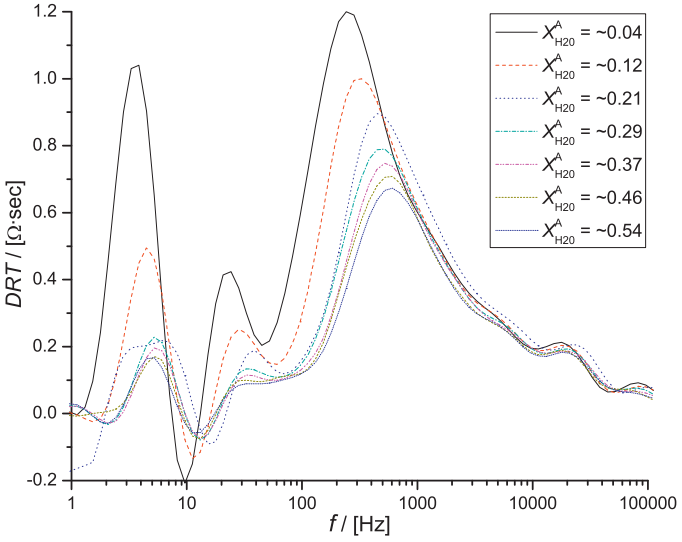

Fig. 16. DRT analysis the impedance measured at OCV, 650 °C and different anode P_{H_2O} (right).

4. Conclusions

We have shown that the perovskite $La_{0.99}Co_{0.4}Ni_{0.6}O_3$ (LCN60) can be used as a SOFC cathode material if mixed into a composite with $Ce_{0.9}Gd_{0.1}O_{1.95}$ (CGO). The performance, measured as R_P at OCV on symmetrical cells is significantly better than the conventional LSM–YSZ, especially at low T due to its low E_A of roughly 1 eV. The performance was improved further by a single wet infiltration of LSC40 nano-particles with R_P of about 270 $m\Omega\,cm^2$ and 440 $m\Omega\,cm^2$ at 600 °C and OCV for the infiltrated and non-infiltrated LCN60–CGO respectively. R_P of the LCN60–CGO cathode was also measured to be remarkably stable compared to reference LSM and LSC based cathodes. The impedance spectra were successfully broken down into an EQC model consisting of a Gerischer impedance (Z_G) and a Z_{RQ} circuit. The low capacitance at OCV of both responses indicated that the electrode processes occur mainly at the electrode surface near the TPB, i.e., bulk diffusion of O^{2-} is not of importance.

The LCN60–CGO cathode was successfully integrated into an anode supported cell. *i–v* polarisation measurements showed a fuel utilization corrected ASR of 0.16–0.18 at 750 °C. EIS measurements showed further that the activity and transport processes of this electrode are such that its contribution to the cell resistance is minor.

Acknowledgement

The authors wish to thank H. Henriksen, M. Davodi, and S. Koch for technical assistance, J. H. Jørgensen for development of software for carrying out DRT analysis, and J. Højberg for assistance with symmetrical cell measurements. Financial support from Energinet.dk through PSO project no. 7124 SOFC R&D.

References

[1] K. Huang, H.Y. Lee, J.B. Goodenough, J. Electrochem. Soc. 145 (1998) 3220–3227.
[2] T. Arunarkavalli, G.U. Kulkarni, C.N.R. Rao, J. Solid State Chem. 107 (1993) 299–301.
[3] T. Saitoh, T. Mizokawa, A. Fujimori, M. Abbate, Y. Takeda, M. Takano, Phys. Rev. B 55 (1997) 4257–4266.
[4] M.A. Senaris-Rodriguez, J.B. Goodenough, J. Solid State Chem. 116 (1995) 224–231.
[5] M. Abbate, J.C. Fuggle, A. Fujimori, L.H. Tjeng, C.T. Chen, R. Potze, G.A. Sawatzky, H. Eisaki, S. Uchida, Phys. Rev. B 47 (1993) 16124–16127.

[6] K. Asai, A. Yoneda, O. Yokokura, J.M. Tranquada, G. Shirane, J. Phys. Soc. Jpn. 67 (1998) 290–296.
[7] M. Hrovat, N. Katsarakis, K. Reichmann, S. Bernik, D. Kuscer, J. Holc, Solid State Ionics 83 (1996) 99–105.
[8] K. Sreedhar, J.M. Honig, M. Darwin, M. Mcelfresh, P.M. Shand, J. Xu, B.C. Crooker, J. Spalek, Phys. Rev. B 46 (1992) 6382–6386.
[9] P. Hjalmarsson, M. Sogaard, A. Hagen, M. Mogensen, Solid State Ionics 179 (2008) 636–646.
[10] L.A. Chick, L.R. Pederson, G.D. Maupin, J.L. Bates, L.E. Thomas, G.J. Exarhos, Mater. Lett. 10 (1990) 6–12.
[11] T.Z. Sholklapper, C. Lu, C.P. Jacobson, S.J. Visco, L.C. De Jonghe, Electrochemi. Solid State Lett. 9 (2006) A376–A378.
[12] P. Plonczak, M. Joost, J. Hjelm, M. Søgaard, M. Lundberg, P.V. Hendriksen, J. Power Sources 196 (2011) 1156–1162.
[13] H. Schichlein, A.C. Müller, M. Voigts, A. Krügel, E. Ivers-Tiffée, J. Appl. Electrochem. 32 (2002) 875–882.
[14] S. Singhal, K. Kendall, Chapter 10: Testing of Electrodes, Cells and Short Stacks, High Temperature Solid Oxide Fuel Cells: Fundamentals, Design and Applications, Elsevier Advanced Technology, Oxford, 2003 (p. 261).
[15] A. Berenov, H. Wood, A. Atkinson, Solid Oxide Fuel Cells 10 (Sofc-X) (2007) 1173–1181 (Pts 1 and 2,7).
[16] S.P. Jiang, J. Mater. Sci. 43 (2008) 6799–6833.
[17] S.R. Wang, M. Katsuki, T. Hashimoto, M. Dokiya, J. Electrochem. Soc. 150 (2003) A952–A958.
[18] D.P. Huang, Q. Xu, W. Chen, H. Wang, R.Z. Yuan, J. Inorg. Mater. 20 (2005) 133–138.
[19] L.W. Tai, M.M. Nasrallah, H.U. Anderson, D.M. Sparlin, S.R. Sehlin, Solid State Ionics 76 (1995) 273–283.
[20] P. Hjalmarsson, M. S°gaard, M. Mogensen, Solid State Ionics 179 (2008) 1422–1426.
[21] X.Y. Chen, J.S. Yu, S.B. Adler, Chem. Mater. 17 (2005) 4537–4546.
[22] M.J.L. Ostergard, M. Mogensen, Electrochim. Acta 38 (1993) 2015–2020.
[23] S.B. Adler, Chem. Rev. 104 (2004) 4791–4843.
[24] S.B. Adler, Solid State Ionics 111 (1998) 125–134.
[25] S.B. Adler, J.A. Lane, B.C.H. Steele, J. Electrochem. Soc. 143 (1996) 3554–3564.
[26] A. Mitterdorfer, L.J. Gauckler, Solid State Ionics 117 (1999) 187–202.
[27] A. Mitterdorfer, L.J. Gauckler, Solid State Ionics 117 (1999) 203–217.
[28] E. Siebert, A. Hammouche, M. Kleitz, Electrochim. Acta 40 (1995) 1741–1753.
[29] H. Schichlein, A.C. Muller, M. Voigts, A. Krugel, E. Ivers-Tiffee, J. Appl. Electrochem. 32 (2002) 875–882.
[30] P. Hjalmarsson, M. Sogaard, M. Mogensen, Solid State Ionics 180 (2009) 1395–1405.
[31] B.A. Boukamp, H.J.M. Bouwmeester, Solid State Ionics 157 (2003) 29–33.
[32] M. Kleitz, F. Petitbon, Solid State Ionics 92 (1996) 65–74.
[33] F. Berthier, J.P. Diard, B. Legorrec, C. Montella, Corrosion 51 (1995) 105–115.
[34] A. Mitterdorfer, L.J. Gauckler, Solid State Ionics 111 (1998) 185–218.
[35] J. Fleig, F.S. Baumann, V. Brichzin, H.R. Kim, J. Jamnik, G. Cristiani, H.U. Habermeier, J. Maier, Fuel Cells 6 (2006) 284–292.
[36] M. Mogensen, Proc.14th Int. Symp. Mater. Sci. (1993) 117–120.
[37] V. Brichzin, J. Fleig, H.U. Habermeier, G. Cristiani, J. Maier, Solid State Ionics 152 (2002) 499–507.
[38] M. Mogensen, M. Søgaard, P. Blennow, K.K. Hansen, Proc. 8th. Eur. Solid Oxide Fuel Cell Forum (2008) A0402.
[39] Y. Teraoka, H. Kakebayashi, I. Moriguchi, S. Kagawa, J. Alloys Compd. 193 (1993) 70–72.
[40] A. Gobichon, J. Auffrédic, D. Louër, Solid State Ionics 93 (1996) 51–64.
[41] I.M. TorresdaSilva, J. Nielsen, J. Hjelm, M. Mogensen, ECS Trans. (SOFC XI) 25 (2009) 489.
[42] T.G. Ramos, J. Hjelm, M. Wandel, A. Hagen, M. Mogensen, ECS Trans. 13 (2008) 235–248.